

Dominant Scattering Mechanisms in Limiting the Electron Mobility of Scandium Nitride

Sourav Rudra, Dheemahi Rao, Samuel Poncé,* and Bivas Saha*

Cite This: *Nano Lett.* 2024, 24, 11529–11536

Read Online

ACCESS |

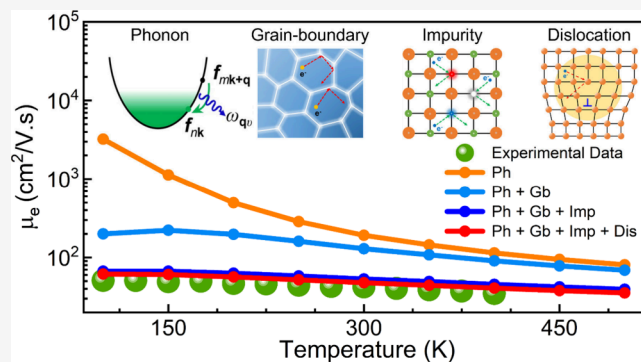
Metrics & More

Article Recommendations

Supporting Information

ABSTRACT: Electron mobility in nitride semiconductors is limited by electron–phonon, defect, grain-boundary, and dislocation scatterings. Scandium nitride (ScN), an emerging rocksalt indirect bandgap semiconductor, exhibits varying electron mobilities depending on growth conditions. Since achieving high mobility is crucial for ScN’s device applications, a microscopic understanding of different scattering mechanisms is extremely important. Utilizing the *ab initio* Boltzmann transport formalism and experimental measurements, here we show the hierarchy of various scattering processes in restricting the electron mobility of ScN. Calculations unveil that though Fröhlich interactions set an intrinsic upper bound for ScN’s electron mobility of $\sim 524 \text{ cm}^2/\text{V}\cdot\text{s}$ at room temperature, ionized-impurity and grain-boundary scatterings significantly reduce mobility. The experimental temperature dependence of mobilities is captured well considering both nitrogen-vacancy and oxygen-substitutional impurities with appropriate ratios, and room-temperature doping dependency agrees well with the empirical Caughey–Thomas model. Furthermore, we suggest modulation doping and polar-discontinuity doping to reduce ionized-impurity scattering in achieving a high-mobility ScN for device applications.

KEYWORDS: electron–phonon coupling, first-principles calculations, carrier transport, Boltzmann transport, ionized-impurity scattering, grain-boundary scattering, dislocation scattering, scandium nitride (ScN)



Electron mobility in semiconductors is typically limited by several scattering processes, such as electron–phonon, ionized-impurity, grain-boundary, and dislocation.^{1,2} While some of these scattering events are intrinsic to the materials, others depend on the geometry, structure, presence of defects, dopants, and other extrinsic conditions. However, irrespective of their origin, these scattering processes reduce electron mobility and degrade electronic, optical, and optoelectronic device performance.³ In the case of nitride semiconductors, the carrier scattering and associated mobility reduction are of particular concern since the deposition of epitaxial and stoichiometric thin films is challenging,^{4–6} and many III-nitride semiconductors exhibit polar bonds leading to electron longitudinal optical (LO) phonon scattering or Fröhlich interactions.^{7–9} Therefore, a microscopic understanding of the intricate details and hierarchy of possible scattering processes is extremely important in the design of high-mobility nitride semiconductors and tuning their electronic transport for device applications.

Scandium nitride (ScN), a promising rocksalt group III(B)-nitride semiconductor, suffers from low electron mobilities compared to its III(A)-nitride counterparts.^{10,11} Moreover, mobility in ScN strongly depends on the growth method and deposition conditions, with values ranging from less than $10 \text{ cm}^2/\text{V}\cdot\text{s}$ to $284 \text{ cm}^2/\text{V}\cdot\text{s}$ at room temperature.^{12,13} ScN is a

corrosion-resistant, mechanically hard, refractory transition metal pnictide and has attracted much interest for thermoelectricity, as a semiconducting component for epitaxial metal/semiconductor superlattices, and as seed layers for defect-free GaN growth.^{11,14} In recent years, ScN thin films have also exhibited low loss and high figure-of-merit infrared plasmon and phonon polaritons and optoelectronic artificial synaptic functionalities that mimic neurons and learning abilities.^{15,16} ScN exhibits an indirect Γ –X bandgap of 0.9 eV, a direct bandgap of $\sim 2.2 \text{ eV}$, and a degenerate semiconducting nature with electron concentration in the 10^{20} – 10^{21} cm^{-3} range.^{11,17} Furthermore, due to its polar nature, the vibrational spectrum of ScN exhibits a large LO transverse optical (TO) phonon mode splitting and the LO phonon mode exhibits the highest energy of $\sim 85 \text{ meV}$ at the Γ -point.^{18,19} Mg hole doping has been used successfully to obtain *p*-type ScN thin films^{20,21} with a maximum hole concentration of $2.2 \times 10^{20} \text{ cm}^{-3}$. Mg-hole-

Received: June 20, 2024

Revised: August 26, 2024

Accepted: September 4, 2024

Published: September 6, 2024



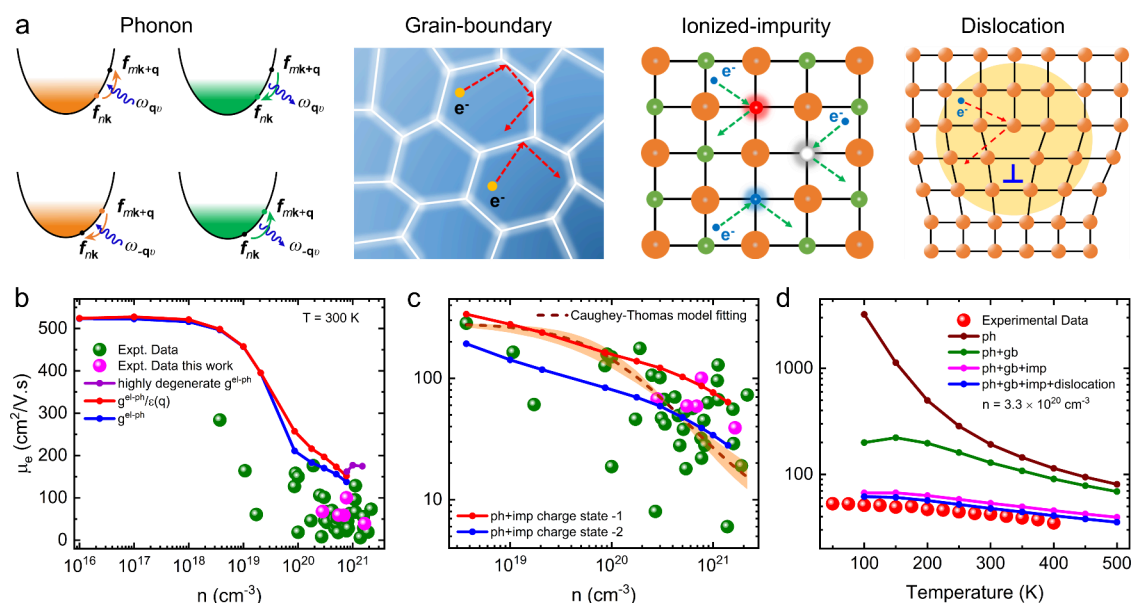


Figure 1. Effect of several scattering mechanisms in limiting electron mobility of ScN. (a) Schematic of electron–phonon, grain-boundary, ionized-impurity, and dislocation scattering in limiting the electron mobility of semiconductors. (b) Experimental Hall mobility (μ_{e}) of electrons in ScN thin films in the existing literature^{12,13,15,19,23,25,27,37–40} (green data points) and experiments from this work (magenta data points), along with the calculated aiBTE phonon-limited room-temperature mobility with and without considering screening of electron–phonon matrix elements as represented by red and blue dots, respectively, as a function of carrier concentrations (n). Mobility remains unchanged for lower electron concentrations as we are in the intrinsic regime with similar electron–phonon scattering rates (Figure S20). In the highly degenerate doping limit, LO phonon frequency decreases due to free carrier screening, which results in increasing mobility, as shown by the purple data points, considering the highly degenerate electron–phonon matrix elements. Calculations are performed on some individual n values of 10^{16} , 10^{17} , 10^{18} , 3.7×10^{18} , 10^{19} , 2.07×10^{19} , 8.65×10^{19} , 1.77×10^{20} , 3×10^{20} , 5×10^{20} , 7.7×10^{20} , 7.8×10^{20} , 10^{21} , and 1.5×10^{21} cm⁻³, respectively. (c) Fitting of experimental room-temperature electron mobility in ScN by the empirical Caughey–Thomas model with calculated electron mobility from aiBTE including Fröhlich interaction and ionized-impurity scattering for two different impurity charge states. Mobility calculations including ionized-impurity scattering are done on n values of 3.7×10^{18} , 10^{19} , 2.07×10^{19} , 8.65×10^{19} , 1.77×10^{20} , 3×10^{20} , 5×10^{20} , 7.7×10^{20} , 10^{21} , and 1.4×10^{21} cm⁻³, respectively. (d) Contribution of different scattering mechanisms to the temperature-dependent electron mobility in n -type ScN with a carrier concentration of 3.3×10^{20} cm⁻³. The calculations are carried out in a temperature range of 100 to 500 K with an interval of 50 K.

doped ScN thin films are also shown to exhibit an intriguing quasi-classical Anderson transition, associated with a 9 order of magnitude increase in their resistivity.²²

Traditionally, magnetron sputtering and molecular beam epitaxy (MBE)-deposited ScN thin films on (001) MgO substrates exhibit maximum room-temperature electron mobility of ~ 90 – 130 cm²/V·s.²³ However, such higher mobility is achieved only in films deposited at high growth temperatures of more than 800 °C and high growth rates (metal-rich growth condition).²³ A decrease in the growth temperature, nitrogen-rich growth conditions, and changes in the substrate orientation or type usually lead to reduced electron mobility as low as 2–5 cm²/V·s at room temperature.^{12,24} Previous microscopic analysis has revealed that ScN thin films deposited with reduced substrate temperature lack sufficient adatom mobilities due to the Ehrlich–Schwoebel barrier that results in V-shaped columnar grain growth with structural voids.²⁵ These columnar grain boundaries and voids act as electron scattering centers, impacting electronic transport. Further, due to a considerable lattice mismatch with (001) MgO and (0001) Al₂O₃ substrates, practically all ScN thin films contain misfit and threading dislocations that provide an unavoidable pathway for electron scattering.^{11,26} Nevertheless, with a large growth rate of a few micrometers per hour, hybrid vapor-phase epitaxy (HVPE) deposited micrometer-thick ScN films exhibit the highest room-temperature electron mobility of 284 cm²/V·s,¹³ suggesting the possibility

of improving the mobility in nanometer-thick films for device applications.

Along with such structural and geometric defects, ionized impurities such as substitutional oxygen, halogen atoms, and nitrogen vacancies are also expected to influence the electronic transport in ScN significantly. Sputtering or MBE-deposited ScN thin films usually contain a significant $\sim 1.6 \pm 1$ atomic % of oxygen (O_N) during the growth process, primarily from source contaminations, which leads to its degenerate electronic nature.²⁷ Theoretical calculations have also shown that the formation of nitrogen vacancies (V_N) is energetically favorable in metal-rich growth conditions, and V_N should act as donors increasing ScN's carrier concentrations.^{28,29} ScN films obtained with HVPE and other types of chemical synthesis methods that utilize halogen-containing reagents have also shown Cl and F impurities acting as donors that scatter electrons, reducing ScN's mobility.^{12,13}

While the Fröhlich interaction presents an intrinsic electron scattering process in ScN that is difficult to overcome, ionized-impurity, grain-boundary, and dislocation scatterings represent extrinsic factors that could be controlled to a larger extent. However, a detailed microscopic understanding of these scattering processes and their relative contributions to the overall mobility reduction are not analyzed with detailed experimental studies or through comprehensive theoretical calculations. Though the electronic structure of ScN has been analyzed over the last two decades with *ab initio* methods such as density functional theory with advanced exchange-

correlation functionals,^{28,30} electron scattering processes, especially ionized-impurity, grain-boundary, and dislocation, are barely investigated. A few recent theoretical calculations have determined the defect formation energy and defect energy states inside ScN's electronic structure; however, no other studies exist except for a single report on the electron–phonon coupling and phonon-limited mobility calculation.³¹ In this work, utilizing the *ab initio* Boltzmann transport equation (aiBTE), the hierarchy of various scattering processes such as electron–phonon, ionized-impurity, grain-boundary, and dislocation scatterings that limit the electron mobility of ScN are determined. Further, we suggest experimental pathways such as modulation doping and polar-discontinuity doping and suitable choices for substrate and growth conditions that are expected to reduce the ionized-impurity, grain-boundary, and dislocation scatterings.

The electron mobility in ScN is modeled hierarchically including major scatterings such as electron–phonon, ionized-impurity, grain-boundary, and dislocation, as shown in Figure 1a. Here, only phonon (considering all phonon modes) and phonon with ionized-impurity scattering limited mobilities are calculated from aiBTE at room temperature.^{32,33} In a hierarchical order, the temperature-dependence of mobility incorporating other scatterings such as grain-boundary and line-charged dislocations are computed using Matthiessen's rule, followed by semiempirical models.^{34–36} Details on the methodology, convergence analysis, and further discussions are presented in the Supporting Information (SI) Section 1.

Calculations show (see Figure 2a) that the Fröhlich interaction dominates the phonon-limited intrinsic room-temperature electronic drift and Hall mobility in ScN with values of 549 and 524 cm²/V·s, respectively, for a carrier concentration of 10¹⁶ cm⁻³. As the Fermi level (E_F) shifts toward the conduction band with the increase in electron concentration, the phonon-limited mobility decreases due to increased scattering phase space near E_F , as shown in Figure 1b (blue dots). However, with the increase in free charge carriers, the Fröhlich interaction is screened, increasing mobility at high carrier concentrations (see red dots in Figure 1b). To account for such screening processes, Lindhard dielectric function under the random phase approximation (RPA) or Thomas–Fermi (TF) screening, a static limit of the Lindhard function with a small wavevector (\mathbf{q}) is utilized.^{33,41} In both these methods, the electron–phonon matrix element is screened by the RPA or TF dielectric constant, such as $g_{mn}(\mathbf{k}, \mathbf{q})/\epsilon(\mathbf{q})$.⁴² Depending on the characteristic plasma frequency of electrons (ω_p) and LO phonon energy (ω_{LO}), TF screening is found effective in the degenerate regime ($n \geq 8 \times 10^{19}$ cm⁻³), while Lindhard screening works best in the nondegenerate limit ($n \leq 2 \times 10^{19}$ cm⁻³) (see SI Section 2).

However, in the highly degenerate regime, characterized by $n \geq 7.8 \times 10^{20}$ cm⁻³, the free electrons inside the conduction band (CB) screen the long-range macroscopic electric field from LO phonon vibrations, increasing the electron mobility further. In this regime, free carrier screening also affects the LO phonon energy and collapses the LO–TO splitting. The LO phonon frequency in ScN quenches with increasing carrier concentration with an effective decrease from 677 to 440 ± 30 cm⁻¹ at higher carrier concentration³⁰ $\sim 1.28 \times 10^{21}$ cm⁻³, which further leads to a significant enhancement of room-temperature electron mobility in the highly degenerate regime, shown in Figure 1b (purple dots). Therefore, phonon-limited intrinsic electron mobility in the ScN ranges from 524 to 177

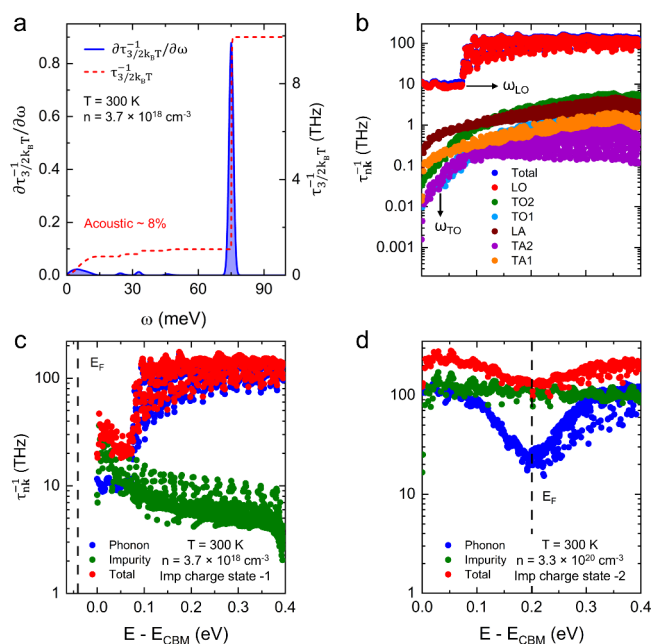


Figure 2. Phonon and ionized-impurity limited scattering rates of electrons in *n*-type ScN. (a) Spectral decomposition of the scattering rates of electrons as a function of phonon energy, calculated at the most representative $3/2k_B T$ away from the conduction band (CB) edge. The red dashed line corresponds to the right-hand vertical axis, representing the cumulative integral of $\partial\tau^{-1}/\partial\omega$ adding up to the carrier scattering rate τ^{-1} . (b) Phonon mode-resolved electron scattering rates as a function of carrier energy with respect to the CB edge. The characteristic frequencies are marked as ω_{LO} and ω_{TO} , corresponding to LO and TO modes at the Γ -point. (c and d) Carrier scattering rates, including both phonon and ionized-impurity scatterings, are represented for carrier concentrations of 3.7×10^{18} cm⁻³ with the impurity charge state “-1” and 3.3×10^{20} cm⁻³ with the impurity charge state “-2”, respectively.

cm²/V·s at room temperature with the increase in electron concentration from 10¹⁶ to 10²¹ cm⁻³.

Experiments show a wide range of room-temperature electron mobility of ScN both in the single crystal and polycrystalline films as a function of electron concentrations (see green dots from literature reports and magenta dots from this work in Figure 1c). The room-temperature experimental mobility with carrier concentration is fitted with the empirical Caughey–Thomas model:⁴³

$$\mu = \frac{\mu_{\max} - \mu_{\min}}{1 + \left(\frac{n}{n_{\text{ref}}}\right)^{\alpha}} + \mu_{\min}$$

The fitting yields a $\mu_{\max} = 284$ cm²/V·s and $\mu_{\min} = 6$ cm²/V·s with α and n_{ref} of 1.09 and 9.86×10^{19} cm⁻³, respectively. The orange-shaded region around the fitted line in Figure 1c includes the error bar of α and n_{ref} in fitting. In addition, as ScN thin films show significantly lower experimental mobility than the limit set by the phonon (see Figure 1b), additional scattering, such as ionized-impurity with different charge states, is incorporated in the modeling. Results show that native defects such as V_N and foreign impurities such as Cl_N and F_N having a charge state of “-1” while O_N donors exhibit a charge state of “-2” drastically reduce mobility from the intrinsic phonon-limited values. Moreover, with the inclusion of ionized-impurity scattering, calculated mobilities become close to the experimental results.

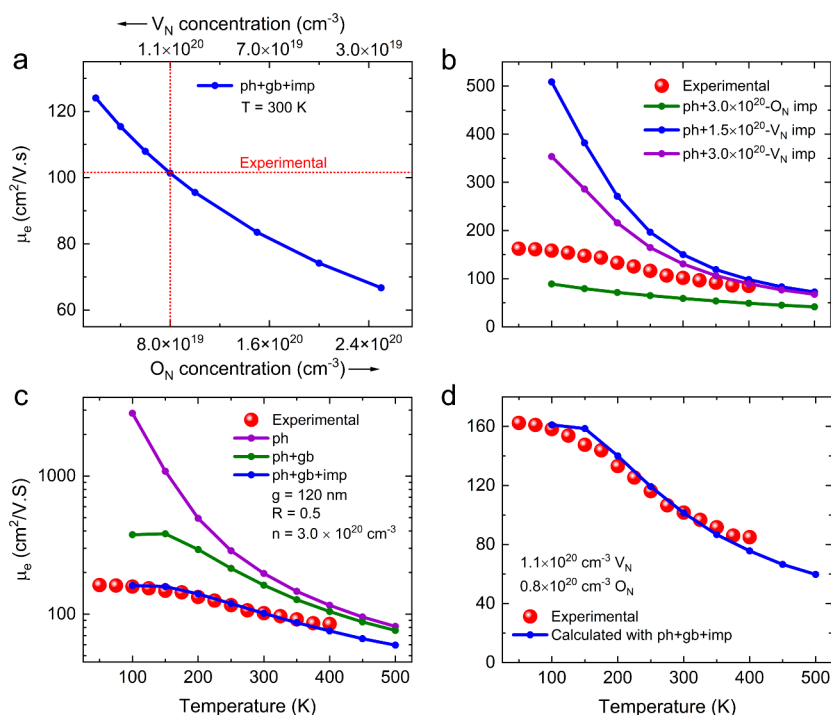


Figure 3. Hierarchy of different scattering processes in limiting the electron mobility of the ScN film with an electron concentration of 3×10^{20} cm⁻³. (a) Effects of the variation of oxygen-impurity (O_N) and nitrogen-vacancy (V_N) point defects on the electron mobility of ScN at room temperature with constant phonon and grain-boundary scattering throughout the varied impurity concentrations. (b) Effect of ionized-impurity scattering on temperature-dependent electron mobility on top of phonon contribution with varied impurity charge states and concentrations. (c) Temperature-dependent electron mobility of the film, including phonon, mixed ionized-impurity of two different types (O_N and V_N) and concentrations, and grain-boundary scattering along with the reported experimental data. (d) Zoomed-in version of the previous temperature-dependent plot in a smaller mobility range. The calculated temperature-dependent mobility, including dominant contributions, shows an excellent agreement with the experimentally reported values.³⁸ The calculations are carried out in a temperature range of 100 to 500 K with an interval of 50 K.

Calculated room-temperature electron mobility considering ionized-impurity scattering with charge state “-1” over the electron–phonon scattering is 337 cm²/V·s for the carrier concentration $\sim 3.7 \times 10^{18}$ cm⁻³, which is close to the experimental report of 284 cm²/V·s for the HVPE deposited ScN. When only the “-2” charge state is considered, mobility decreases lower than the experimental value, highlighting that halide contaminations are the major impurity scattering in lowering phonon-limited mobility for those HVPE films. Similarly, in the high carrier concentration range (10^{20} – 10^{21} cm⁻³), the electron mobility of MBE and sputter-deposited ScN films agree well with substitutional oxygen with a “-2” charge state as the major ionized-impurity scattering center. Therefore, the region encompassed by red and blue boundaries in Figure 1c shows the regime where along with Fröhlich dominated interactions, ionized-impurity scattering from mixed charge states is present.

Although most ScN films exhibit electron mobility that is close to the limit set by the “-2” impurity charge state (blue curve in Figure 1c), some show lower values, highlighting the presence of other scattering mechanisms, such as grain-boundary and dislocation scatterings. The inclusion of grain-boundary and dislocation scatterings in the overall mobility expression fits the experimental temperature-dependent electron mobility¹⁵ for carrier concentration $\sim 3.3 \times 10^{20}$ cm⁻³ quite well, as shown in Figure 1d. The low-temperature plateau in the experimental mobility appears mainly due to the increased grain-boundary scattering as the electronic mean free path at low-temperature is larger than the grain size. Therefore,

these calculations establish a clear hierarchy of different scattering mechanisms that reduce the electron mobility of ScN films.

Spectrally decomposed phonon-limited scattering rates of electrons at $3/2k_B T$ away from CB show a sharp peak at 75 meV (ω_{LO}), suggesting strong Fröhlich interactions and a small contribution of $\sim 8\%$ from acoustic phonons (see Figure 2a), which is further validated with the mode-resolved scatterings. Optical phonon scatterings in ScN are inelastic with activation thresholds (see Figure 2b). Above the threshold, both emission and absorption of optical phonons increase, which leads to an enhanced electron–phonon scattering. Incorporating ionized-impurity scattering further increases the scattering rates (see Figures 2c and 2d) with a dip near E_F in the degenerate carrier limit ($\sim 3.3 \times 10^{20}$ cm⁻³) for LO phonon scattering.⁴⁴ The room-temperature relaxation time of electrons around E_F , including both the scatterings, yields 7.6 fs in close agreement with the experimentally reported value of 9 fs.¹⁵ Further, the effect of scatterings from different impurity charge states on electron mobility having similar carrier concentrations are compared (see SI Section 6).

Depending on growth conditions, MBE and sputter-deposited ScN films with similar carrier concentrations can show significantly different electron mobilities. For example, films having a carrier concentration of $\sim 3.0 \times 10^{20}$ cm⁻³ exhibit a high electron mobility of 101 cm²/V·s when deposited with metal-rich growth conditions,³⁸ while films exhibiting electron concentrations of $\sim 3.3 \times 10^{20}$ cm⁻³ deposited with lesser metal flux exhibit lower mobility of 43

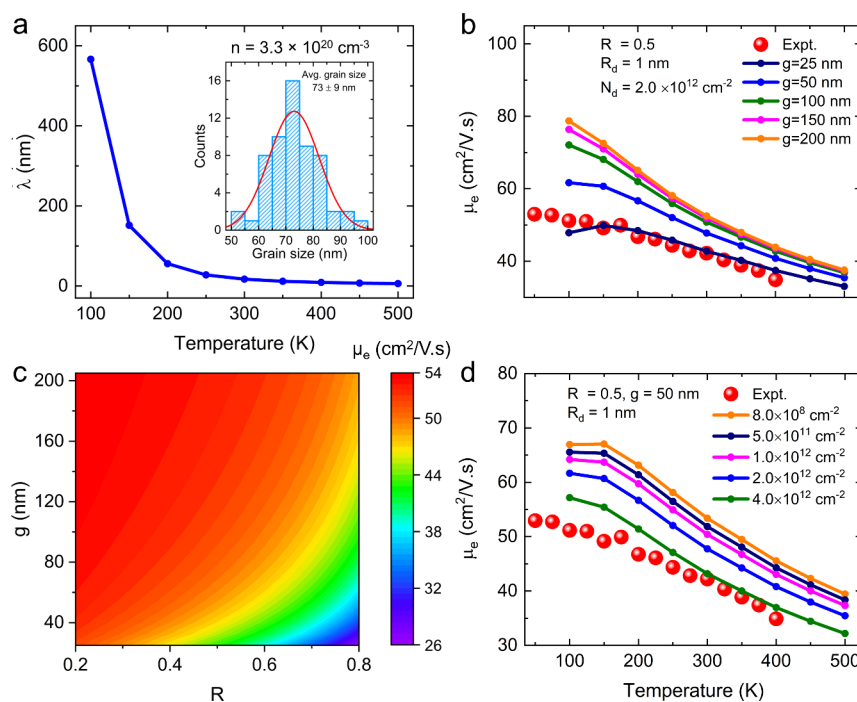


Figure 4. Dependence of the grain-boundary and dislocation scattering parameters to the temperature dependence of the ScN's electron mobility with an experimental¹⁵ carrier concentration of $3.3 \times 10^{20} \text{ cm}^{-3}$. (a) Temperature-dependent *ab initio* transport mean free path (λ) of the electron in *n*-type ScN. The inset shows the scanning electron microscopy histogram of the grain size distribution of the ScN film with an average grain size of 73 nm. (b) The effect of grain size variation on the grain-boundary scattering while considering other scattering parameters to be fixed. (c) Room-temperature electron mobility of ScN as a function of varying both the grain size (g in nm) and coefficient of reflection (R) from grains. (d) The effect of dislocation density variation on the electron mobility of ScN while keeping other scattering parameters constant. The unit of dislocation density is in cm^{-2} . The calculations are carried out in a temperature range of 100 to 500 K with an interval of 50 K.

$\text{cm}^2/\text{V}\cdot\text{s}$.¹⁵ Usually, metal-rich growth conditions lead to faster growth rates,⁴⁵ reducing the relative concentration of O_N in the films.⁴⁶ These results indicate the presence of both O_N and V_N simultaneously in the films. To understand this behavior, changes in the electron mobility of ScN with increasing (decreasing) O_N (V_N) concentrations in the full ionization limit are calculated. The result shows (see Figures 3a and 3b) the relative dominance of O_N over V_N in reducing mobility. The O_N and V_N concentrations are not known for the experimental room-temperature Hall mobility of $\sim 101 \text{ cm}^2/\text{V}\cdot\text{s}$. Based on our simulation results in Figure 3a, the data suggests the presence of $1.1 \times 10^{20} \text{ cm}^{-3}$ V_N and $0.8 \times 10^{20} \text{ cm}^{-3}$ O_N concentrations in the film.

This is further manifested with the temperature-dependent mobility calculations, where the experimental results can only be captured with a combination of both types of defects (shown in Figure 3b). Further, Figure 3b shows that although temperature-dependent mobility above room-temperature can be well explained by including phonon and ionized-impurity scatterings, calculations significantly overestimate experimental mobility at lower temperatures. It suggests the presence of additional scattering channels, such as grain-boundary, in reducing mobility. Keeping the ionized-impurity concentration (as marked in Figure 3a) constant, grain-boundary scattering with an effective grain size of 120 nm (see Figure S11) and reflection coefficient of 0.5 captures the experimental temperature-dependent mobility well (see Figure 3c). The little deviation in the higher temperature range (see Figure 3d) is due to considering constant impurity concentrations throughout the simulated temperature range (100–500 K). Therefore, the above calculations suggest that the overall electron mobility

in ScN films results from the combination of mixed ionized-impurity and grain-boundary scatterings.

Further, parameters affecting the grain-boundary and dislocation scattering limited mobility in ScN are investigated by using empirical models. Grain-boundary scattering depends on carrier mean free path (λ), grain size (g), and reflection coefficient (R) from grain boundaries (see SI Section 5).^{34,35} *Ab initio* calculation yields a phonon-limited λ of 18 nm at room temperature in ScN, consistent with the previous findings of 23 nm in a similar carrier concentration range.²⁷ Grain boundary scattering in ScN is significant at lower temperatures due to higher λ (see Figure 4a) as compared to an average grain size of ~ 73 nm obtained from analyzing scanning electron microscopy images (see the inset of Figure 4a). Keeping all other scattering parameters constant, the variation in grain size shows that the scattering rate increases as the grain size reduces. A small grain size of 25 nm captures the temperature-dependent electron mobility well, while a slight deviation is observed at low temperatures (Figure 4b). However, variations of both R and g (shown in Figure 4c) show that room-temperature mobility changes from $26 \text{ cm}^2/\text{V}\cdot\text{s}$ with $g = 25$ nm and $R = 0.8$ to $54 \text{ cm}^2/\text{V}\cdot\text{s}$ with $g = 205$ nm and $R = 0.2$. Depending on growth conditions, dislocations can further lower the mobility of ScN films. High-angle annular dark-field scanning transmission electron microscopy imaging (HAADF-STEM) reveals the presence of threading dislocations in ScN films, which can be considered as line-charged scattering centers (see SI Section 4). Calculation shows that experimental temperature dependence of mobility is captured well for a dislocation density (N_d) of $\sim 4.0 \times 10^{12} \text{ cm}^{-2}$ and a

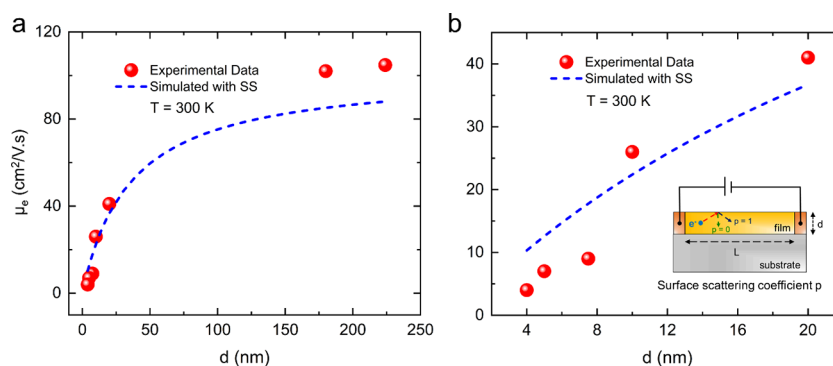


Figure 5. Effect of surface scattering on ScN's electron mobility with reducing film thickness. (a) Thickness-dependent experimental³⁸ and simulated room-temperature electron mobility of ScN films from the Fuchs–Sondheimer (FS) model of surface scattering (SS). (b) Simulated electron mobility of ScN in the ultrathin region agrees well with the experimental trends.

dislocation core radius (R_d) of ~ 1 nm, keeping g and R to be 50 nm and 0.5, respectively (shown in Figure 4d).

Finally, the thickness-dependent electronic transport in ultrathin ScN is determined. Below a critical film thickness ($d < \lambda$), the electrons primarily encounter surface scattering as described by the Fuchs–Sondheimer (FS) model. This model quantifies surface scattering by the phenomenological specular parameter p with both diffuse ($p = 0$) and specular ($p = 1$) limits.⁴⁷ A recent experiment on ultrathin ScN revealed a nearly diffuse scattering behavior. This diffuse surface scattering drastically reduces in-plane electron mobility by randomizing momentum parallel to the surface. As the thickness decreases, the in-plane mobility of ScN drops from its bulk limit ($\mu_B \approx 101$ cm²/V·s), evident for films with thicknesses below λ (~ 18 nm). Under the diffuse surface scattering limit of the FS model, calculated thickness-dependent electron mobility using *ab initio* determined parameters aligns with the experimental mobilities for ultrathin films (see Figures 5a and 5b). However, surface scatterings can be reduced to achieve higher mobility in ultrathin films by minimizing surface roughness through growth mode adjustments, offering an avenue for future experimental research.

Having determined the dominant scattering mechanisms that reduce electron mobility, we also suggest experimental pathways to increase electron mobility in ScN. Improving crystalline quality by high-temperature growth, reducing surface roughness, and growth on nearly lattice-matched substrates such as wurtzite GaN (000 $\bar{1}$) and rocksalt ternary nitride MgHfN₂ (001) will be crucial in reducing the grain boundary, surface states, and dislocation scatterings.^{14,25,26,48} Further, reducing the level of O_N using a high-purity Sc target and metal-rich and high growth rate deposition conditions in an ultra-high-vacuum growth chamber can significantly mitigate the dominant ionized-impurity scatterings. Additionally, advanced engineering methods such as modulation doping and polar-discontinuity doping can be used to decouple the semiconductor channel conductance from the impurity band pinned in the barrier material by forming a 2D-electron gas at the heterostructure interface, such as ScN/GaN (000 $\bar{1}$), which will significantly reduce impurity scattering (see SI Section 7).^{1,49,50} With all such engineering techniques, achieving higher electron mobility of ScN that is greater than Si in the degenerate carrier concentration limit ($\sim 10^{20}$ cm⁻³) may be possible,¹² which will significantly advance ScN's utility in high-performance electronic and optoelectronic applications.

In conclusion, utilizing the *ab initio* Boltzmann transport equation and empirical models for electron–phonon interaction, ionized-impurity, grain-boundary, and dislocation scatterings, we demonstrate the hierarchy of various scattering channels in reducing the electron mobility of ScN. Due to its polar nature, Fröhlich interactions present an intrinsic upper limit to the electron mobility of ScN with values ranging from 524 to 177 cm²/V·s in a 10^{16} to 10^{21} cm⁻³ electron concentration range. Further reduction of mobility in experimental films is caused by ionized-impurity scattering with different charge states, grain boundaries, and dislocation scatterings. The average room-temperature electron mobility with doping concentration aligns with the empirical Caughey–Thomas model. Our comprehensive calculations and analysis show the detailed scattering mechanisms that shape the electronic transport properties of ScN. This work will lead to a better understanding of the scattering parameters to achieve high-mobility ScN films for applications in electronic, thermoelectric, and optoelectronic devices with higher efficiency.

■ ASSOCIATED CONTENT

Data Availability Statement

The data that supports the findings of this study are available from the corresponding author upon reasonable request.

Supporting Information

The Supporting Information is available free of charge at <https://pubs.acs.org/doi/10.1021/acs.nanolett.4c02920>.

Details of computational methods, screening effects in phonon and ionized-impurity scatterings, thin film growth conditions, electrical measurements, FESEM and HRTEM imaging, and detailed analysis of the results (PDF)

■ AUTHOR INFORMATION

Corresponding Authors

Samuel Poncé – European Theoretical Spectroscopy Facility, Institute of Condensed Matter and Nanosciences, Université catholique de Louvain, B-1348 Louvain-la-Neuve, Belgium; WEL Research Institute, 1300 Wavre, Belgium; Email: samuel.ponce@uclouvain.be

Bivas Saha – Chemistry and Physics of Materials Unit, International Centre for Materials Science, and School of Advanced Materials (SAMat), Jawaharlal Nehru Centre for Advanced Scientific Research, Bangalore 560064, India;

orcid.org/0000-0002-0837-1506; Email: bsaha@jncasr.ac.in, bivas.mat@gmail.com

Authors

Sourav Rudra – Chemistry and Physics of Materials Unit and International Centre for Materials Science, Jawaharlal Nehru Centre for Advanced Scientific Research, Bangalore 560064, India

Dheemahi Rao – Chemistry and Physics of Materials Unit and International Centre for Materials Science, Jawaharlal Nehru Centre for Advanced Scientific Research, Bangalore 560064, India; orcid.org/0000-0002-1952-3210

Complete contact information is available at:

<https://pubs.acs.org/10.1021/acs.nanolett.4c02920>

Author Contributions

S.R. and B.S. conceived this project. S.R. performed all the calculations with assistance from S.P. and B.S. D.R. analyzed the electron microscopy imaging obtained from FESEM and HRTEM. S.R., S.P., and B.S. analyzed the results. All authors discussed and contributed to the preparation of the manuscript.

Notes

The authors declare no competing financial interest.

ACKNOWLEDGMENTS

S.R., D.R., and B.S. acknowledge the support of the International Centre for Materials Science (ICMS) and Sheikh Saqr Laboratory (SSL) in JNCASR. S.P. acknowledges the Fonds de la Recherche Scientifique de Belgique (F.R.S.-FNRS) and the Walloon Region in the strategic axe FRFS-WEL-T for financial support. B.S. acknowledges the Science and Engineering Research Board (SERB) of the Government of India, Start-Up Research Grant SRG/2019/000613 for financial support. S.R. thanks the Council of Scientific & Industrial Research (CSIR) for the fellowship. D.R. thanks JNCASR for the fellowship. S.R. and B.S. gratefully acknowledge the support and resources provided by PARAM Yukti Facility under the National Supercomputing Mission (NSM), Government of India at the Jawaharlal Nehru Centre for Advanced Scientific Research (JNCASR) Bangalore. D.R. acknowledges the SAMat research facilities. S.R. and D.R. also acknowledge Mr. Debmalaya Mukhopadhyay for his helping contribution during the thin film deposition. S.R. acknowledges Mr. Prasanna Das for giving suggestions to make the Table of Contents image.

REFERENCES

(1) Yu, P. Y.; Cardona, M. *Fundamentals of Semiconductors; Graduate Texts in Physics*; Springer: Berlin, Heidelberg, 2010; pp 28. DOI: 10.1007/978-3-642-00710-1.

(2) Sommer, N.; Hüpkes, J.; Rau, U. Field Emission at Grain Boundaries: Modeling the Conductivity in Highly Doped Polycrystalline Semiconductors. *Phys. Rev. Appl.* **2016**, *5* (2), No. 024009.

(3) Amano, H.; Baines, Y.; Beam, E.; Borga, M.; Bouchet, T.; Chalker, P. R.; Charles, M.; Chen, K. J.; Chowdhury, N.; Chu, R.; De Santi, C.; De Souza, M. M.; Decoutere, S.; Di Cioccio, L.; Eckardt, B.; Egawa, T.; Fay, P.; Freedman, J. J.; Guido, L.; Häberlen, O.; Haynes, G.; Heckel, T.; Hemakumara, D.; Houston, P.; Hu, J.; Hua, M.; Huang, Q.; Huang, A.; Jiang, S.; Kawai, H.; Kinzer, D.; Kuball, M.; Kumar, A.; Lee, K. B.; Li, X.; Marcon, D.; März, M.; McCarthy, R.; Meneghesso, G.; Meneghini, M.; Morvan, E.; Nakajima, A.; Narayanan, E. M. S.; Oliver, S.; Palacios, T.; Piedra, D.; Plissonnier, M.; Reddy, R.; Sun, M.; Thayne, I.; Torres, A.; Trivellin, N.; Unni, V.; Uren, M. J.; Van Hove, M.; Wallis, D. J.; Wang, J.; Xie, J.; Yagi, S.;

Yang, S.; Youtsey, C.; Yu, R.; Zanoni, E.; Zeltner, S.; Zhang, Y. The 2018 GaN Power Electronics Roadmap. *J. Phys. D: Appl. Phys.* **2018**, *51* (16), 163001.

(4) Gao, Y.; Sun, D.; Jiang, X.; Zhao, J. Point Defects in Group III Nitrides: A Comparative First-Principles Study. *J. Appl. Phys.* **2019**, *125* (21), 215705.

(5) Balasubramanian, K.; Khare, S. V.; Gall, D. Energetics of Point Defects in Rocksalt Structure Transition Metal Nitrides: Thermodynamic Reasons for Deviations from Stoichiometry. *Acta Mater.* **2018**, *159*, 77–88.

(6) Panjan, P.; Drnovšek, A.; Gselman, P.; Čekada, M.; Panjan, M. Review of Growth Defects in Thin Films Prepared by PVD Techniques. *Coatings* **2020**, *10* (5), 447.

(7) Fröhlich, H. Electrons in Lattice Fields. *Adv. Phys.* **1954**, *3* (11), 325–361.

(8) Verdi, C.; Giustino, F. Fröhlich Electron-Phonon Vertex from First Principles. *Phys. Rev. Lett.* **2015**, *115* (17), No. 176401.

(9) Poncé, S.; Jena, D.; Giustino, F. Route to High Hole Mobility in GaN via Reversal of Crystal-Field Splitting. *Phys. Rev. Lett.* **2019**, *123* (9), No. 096602.

(10) Ridley, B. K.; Foutz, B. E.; Eastman, L. F. Mobility of Electrons in Bulk GaN and Al_xGa_{1-x}N/GaN Heterostructures. *Phys. Rev. B* **2000**, *61* (24), 16862–16869.

(11) Biswas, B.; Saha, B. Development of Semiconducting ScN. *Phys. Rev. Mater.* **2019**, *3* (2), No. 020301.

(12) Dismukes, J.; Yim, W.; Ban, V. Epitaxial Growth and Properties of Semiconducting ScN. *J. Cryst. Growth* **1972**, *13–14*, 365–370.

(13) Oshima, Y.; Villora, E. G.; Shimamura, K. Hydride Vapor Phase Epitaxy and Characterization of High-Quality ScN Epilayers. *J. Appl. Phys.* **2014**, *115* (15), No. 153508.

(14) Moram, M. A.; Zhang, Y.; Kappers, M. J.; Barber, Z. H.; Humphreys, C. J. Dislocation Reduction in Gallium Nitride Films Using Scandium Nitride Interlayers. *Appl. Phys. Lett.* **2007**, *91* (15), 8–11.

(15) Maurya, K. C.; Rao, D.; Acharya, S.; Rao, P.; Pillai, A. I. K.; Selvaraja, S. K.; Garbrecht, M.; Saha, B. Polar Semiconducting Scandium Nitride as an Infrared Plasmon and Phonon-Polaritonic Material. *Nano Lett.* **2022**, *22* (13), 5182–5190.

(16) Rao, D.; Pillai, A. I. K.; Garbrecht, M.; Saha, B. Scandium Nitride as a Gateway III-Nitride Semiconductor for Both Excitatory and Inhibitory Optoelectronic Artificial Synaptic Devices. *Adv. Electron. Mater.* **2023**, *9* (3), 2200975.

(17) Al-Brithen, H. A.; Smith, A. R.; Gall, D. Surface and Bulk Electronic Structure of ScN (001) Investigated by Scanning Tunneling Microscopy/Spectroscopy and Optic. *Phys. Rev. B* **2004**, *70* (4), No. 045303.

(18) Paudel, T. R.; Lambrecht, W. R. L. Calculated Phonon Band Structure and Density of States and Interpretation of the Raman Spectrum in Rocksalt ScN. *Phys. Rev. B* **2009**, *79* (8), No. 085205.

(19) Uchiyama, H.; Oshima, Y.; Patterson, R.; Iwamoto, S.; Shiomi, J.; Shimamura, K. Phonon Lifetime Observation in Epitaxial ScN Film with Inelastic X-Ray Scattering Spectroscopy. *Phys. Rev. Lett.* **2018**, *120* (23), No. 235901.

(20) Saha, B.; Garbrecht, M.; Perez-Taborda, J. A.; Fawey, M. H.; Koh, Y. R.; Shakouri, A.; Martin-Gonzalez, M.; Hultman, L.; Sands, T. D. Compensation of Native Donor Doping in ScN: Carrier Concentration Control and *p*-Type ScN. *Appl. Phys. Lett.* **2017**, *110* (25), 252104.

(21) Rudra, S.; Rao, D.; Poncé, S.; Saha, B. Reversal of Band-Ordering Leads to High Hole Mobility in Strained *p*-Type Scandium Nitride. *Nano Lett.* **2023**, *23* (17), 8211–8217.

(22) Rao, D.; Panda, D. P.; Pillai, A. I. K.; Tayal, A.; Garbrecht, M.; Saha, B. Quasiclassical Anderson Transition and Thermally Activated Percolative Charge Transport in Single-Crystalline ScN. *Phys. Rev. B* **2024**, *109* (15), No. 155307.

(23) Ohgaki, T.; Watanabe, K.; Adachi, Y.; Sakaguchi, I.; Hishita, S.; Ohashi, N.; Haneda, H. Electrical Properties of Scandium Nitride Epitaxial Films Grown on (100) Magnesium Oxide Substrates by Molecular Beam Epitaxy. *J. Appl. Phys.* **2013**, *114* (9), 093704.

- (24) Moustakas, T. D.; Molnar, R. J.; Dismukes, J. P. Growth of Polycrystalline Scandium Nitride by ECR-MBE. *Proc. Electrochem. Soc.* **1996**, *96*, 197.
- (25) Rao, D.; Biswas, B.; Acharya, S.; Bhatia, V.; Pillai, A. I. K.; Garbrecht, M.; Saha, B. Effects of Adatom Mobility and Ehrlich–Schwoebel Barrier on Heteroepitaxial Growth of Scandium Nitride (ScN) Thin Films. *Appl. Phys. Lett.* **2020**, *117* (21), n/a.
- (26) le Febvrier, A.; Tureson, N.; Stalkerich, N.; Greczynski, G.; Eklund, P. Effect of Impurities on Morphology, Growth Mode, and Thermoelectric Properties of (111) and (001) Epitaxial-like ScN Films. *J. Phys. D: Appl. Phys.* **2019**, *52* (3), No. 035302.
- (27) Burmistrova, P. V.; Maassen, J.; Favaloro, T.; Saha, B.; Salamat, S.; Rui Koh, Y.; Lundstrom, M. S.; Shakouri, A.; Sands, T. D. Thermoelectric Properties of Epitaxial ScN Films Deposited by Reactive Magnetron Sputtering onto MgO(001) Substrates. *J. Appl. Phys.* **2013**, *113* (15), 153704.
- (28) Kumagai, Y.; Tsunoda, N.; Oba, F. Point Defects and *p*-Type Doping in ScN from First Principles. *Phys. Rev. Appl.* **2018**, *9* (3), No. 034019.
- (29) Kerdsonpanya, S.; Alling, B.; Eklund, P. Effect of Point Defects on the Electronic Density of States of ScN Studied by First-Principles Calculations and Implications for Thermoelectric Properties. *Phys. Rev. B* **2012**, *86* (19), No. 195140.
- (30) Deng, R.; Ozsdolay, B. D.; Zheng, P. Y.; Khare, S. V.; Gall, D. Optical and Transport Measurement and First-Principles Determination of the ScN Band Gap. *Phys. Rev. B* **2015**, *91* (4), No. 045104.
- (31) Mu, S.; Rowberg, A. J. E.; Leveillee, J.; Giustino, F.; Van De Walle, C. G. First-Principles Study of Electron Transport in ScN. *Phys. Rev. B* **2021**, *104* (7), No. 075118.
- (32) Leveillee, J.; Zhang, X.; Kioupakis, E.; Giustino, F. Ab Initio Calculation of Carrier Mobility in Semiconductors Including Ionized-Impurity Scattering. *Phys. Rev. B* **2023**, *107* (12), No. 125207.
- (33) Lee, H.; Poncé, S.; Bushick, K.; Hajinazar, S.; Lafuente-Bartolome, J.; Leveillee, J.; Lian, C.; Lihm, J.-M.; Macheda, F.; Mori, H.; Paudyal, H.; Sio, W. H.; Tiwari, S.; Zacharias, M.; Zhang, X.; Bonini, N.; Kioupakis, E.; Margine, E. R.; Giustino, F. Electron-Phonon Physics from First Principles Using the EPW Code. *npj Comput. Mater.* **2023**, *9* (1), 156.
- (34) Mayadas, A. F.; Shatzkes, M. Electrical-Resistivity Model for Polycrystalline Films: The Case of Arbitrary Reflection at External Surfaces. *Phys. Rev. B* **1970**, *1* (4), 1382–1389.
- (35) Xia, C. Q.; Peng, J.; Poncé, S.; Patel, J. B.; Wright, A. D.; Crothers, T. W.; Uller Rothmann, M.; Borchert, J.; Milot, R. L.; Kraus, H.; Lin, Q.; Giustino, F.; Herz, L. M.; Johnston, M. B. Limits to Electrical Mobility in Lead-Halide Perovskite Semiconductors. *J. Phys. Chem. Lett.* **2021**, *12* (14), 3607–3617.
- (36) Li, S. S. *Semiconductor Physical Electronics*; Springer: New York, NY, 2006. DOI: 10.1007/0-387-37766-2.
- (37) Al-Atabi, H.; Zheng, Q.; Cetnar, J. S.; Look, D.; Cahill, D. G.; Edgar, J. H. Properties of Bulk Scandium Nitride Crystals Grown by Physical Vapor Transport. *Appl. Phys. Lett.* **2020**, *116* (13), 132103.
- (38) Mukhopadhyay, D.; Rudra, S.; Biswas, B.; Das, P.; Saha, B. Surface Scattering-Dependent Electronic Transport in Ultrathin Scandium Nitride Films. *Appl. Phys. Lett.* **2023**, *123* (19), 192101.
- (39) Rao, D.; Biswas, B.; Flores, E.; Chatterjee, A.; Garbrecht, M.; Koh, Y. R.; Bhatia, V.; Pillai, A. I. K.; Hopkins, P. E.; Martin-Gonzalez, M.; Saha, B. High Mobility and High Thermoelectric Power Factor in Epitaxial ScN Thin Films Deposited with Plasma-Assisted Molecular Beam Epitaxy. *Appl. Phys. Lett.* **2020**, *116* (15), 152103.
- (40) Cetnar, J. S.; Reed, A. N.; Badescu, S. C.; Vangala, S.; Smith, H. A.; Look, D. C. Electronic Transport in Degenerate (100) Scandium Nitride Thin Films on Magnesium Oxide Substrates. *Appl. Phys. Lett.* **2018**, *113* (19), 192104.
- (41) Verdi, C.; Caruso, F.; Giustino, F. Origin of the Crossover from Polarons to Fermi Liquids in Transition Metal Oxides. *Nat. Commun.* **2017**, *8* (1), 15769.
- (42) Giustino, F. Electron-Phonon Interactions from First Principles. *Rev. Mod. Phys.* **2017**, *89* (1), No. 015003.
- (43) Caughey, D. M.; Thomas, R. E. Carrier Mobilities in Silicon Empirically Related to Doping and Field. *Proc. IEEE* **1967**, *55* (12), 2192–2193.
- (44) Krishnaswamy, K.; Himmetoglu, B.; Kang, Y.; Janotti, A.; Van De Walle, C. G. First-Principles Analysis of Electron Transport in BaSnO₃. *Phys. Rev. B* **2017**, *95* (20), No. 205202.
- (45) Smith, A. R.; AL-Britthen, H. A. H.; Ingram, D. C.; Gall, D. Molecular Beam Epitaxy Control of the Structural, Optical, and Electronic Properties of ScN(001). *J. Appl. Phys.* **2001**, *90* (4), 1809–1816.
- (46) Casamento, J.; Xing, H. G.; Jena, D. Oxygen Incorporation in the Molecular Beam Epitaxy Growth of Sc_xGa_{1-x}N and Sc_xAl_{1-x}N. *Phys. status solidi* **2020**, *257* (4), 1–4.
- (47) Gall, D. The Search for the Most Conductive Metal for Narrow Interconnect Lines. *J. Appl. Phys.* **2020**, *127* (5), 050901.
- (48) Bauers, S. R.; Holder, A.; Sun, W.; Melamed, C. L.; Woods-Robinson, R.; Mangum, J.; Perkins, J.; Tumas, W.; Gorman, B.; Tamboli, A.; Ceder, G.; Lany, S.; Zakutayev, A. Ternary Nitride Semiconductors in the Rocksalt Crystal Structure. *Proc. Natl. Acad. Sci. U. S. A.* **2019**, *116* (30), 14829–14834.
- (49) Krishnaswamy, K.; Bjaalie, L.; Himmetoglu, B.; Janotti, A.; Gordon, L.; Van de Walle, C. G. BaSnO₃ as a Channel Material in Perovskite Oxide Heterostructures. *Appl. Phys. Lett.* **2016**, *108* (8), 083501.
- (50) Adamski, N. L.; Dreyer, C. E.; Van de Walle, C. G. Giant Polarization Charge Density at Lattice-Matched GaN/ScN Interfaces. *Appl. Phys. Lett.* **2019**, *115* (23), 232103.